PERFORMANCE AND LIFE CYCLE COST COMPARISON OF OPTIMIZED FIXED-WING VTOL UAV CONFIGURATIONS

P. Stahl, C. Roessler, M. Hornung,
Institute of Aircraft Design, Technical University of Munich,
Boltzmannstraße 15, 85748 Garching, Germany

Abstract

Fixed-wing VTOL UAV are unmanned aerial vehicles capable of both hover and fast forward flight. A variety of aircraft layouts are imaginable which provide these capabilities. To answer the question for the best layout for a specific application, a fixed-wing VTOL aircraft preliminary design tool was implemented and extended by a cost analysis. While aerodynamic, structural and system sizing, performance estimation and mass modelling rely on conventional techniques, e.g. the interaction of rotor/propeller flow with wing and fuselage is fixed-wing VTOL specific. Due to the sensitivity of an all-electric aircraft on power supply, battery modelling is a given special focus. Four fixed-wing VTOL configurations were implemented and compared. For comparison, all four aircraft were optimized by varying of their basic geometry parameters. The resulting performance and cost breakdowns not only reveal the best 5kg-class aircraft for the exemplary land survey mission, it also sets the basis to judge on the economic profitability of the UAV application.

Keywords

UAV; fixed-wing; VTOL; electric; design; performance; life cycle cost

1. INTRODUCTION

Multirotor and fixed-wing UAV are already in use for tasks like aerial filming, surveillance, photogrammetric survey, etc. Multirotor systems offer the capability of take-off and landing in confined environments but cannot provide enough range and endurance for certain missions. Fixed-wing UAV offer the latter but require space and infrastructure for take-off and landing. Fixed-wing VTOL UAV try to close this gap. They can operate in a powered lift mode for take-off and landing and in a wing-borne forward flight mode. To add VTOL capabilities to a fixed-wing aircraft a wide range of aircraft layouts are imaginable. These configurations distinguish themselves in the type of the basic fixed-wing aircraft, type and positioning of the hover propulsion system, grade of functionality share, etc.

To answer the question 'Which fixed-wing VTOL configuration is the best for a certain application?', different fixed-wing VTOL configurations are designed and optimized using an automated preliminary aircraft design framework. The common practice of evaluating an aircraft design solely based on a tool's performance results neglects large parts of the environment the aircraft is actually operated in. Connecting a life cycle cost model to the above design tool allows to evaluate the initial question from a more holistic, economic perspective.

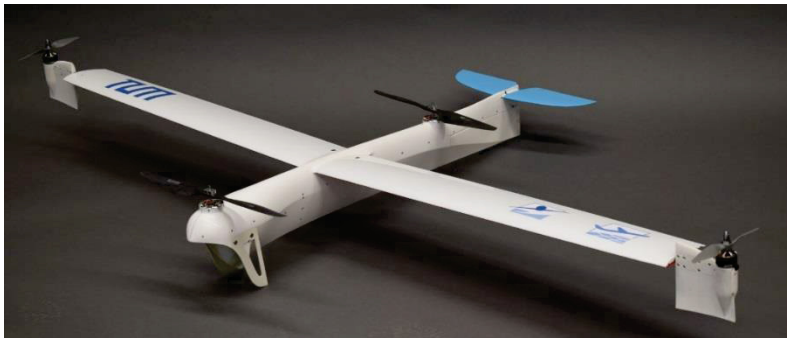

FIG 1. Exemplary 'quadPtilt' Configuration, Developed at Institute of Aircraft Design/TU Munich

2. PRELIMINARY AIRCRAFT DESIGN TOOL AND COST MODEL

2.1. Objective and Limitations of the Tool

The tool focuses on unmanned fixed-wing VTOL aircraft up to 50 kg take-off mass with conventional wing-tail configuration and purely electric powertrains. The comparison of aircraft configurations as well as the impact evaluation of novel subsystems (e.g. rotor housing for drag reduction) on the overall aircraft represent a main goal of the tool. The methods as well as the overall structure allow for fast and flexible implementation of new fixed-wing VTOL configurations, especially their powertrain arrangement. Furthermore, it serves as a first computational step in fixed-wing VTOL UAV design. It copes with minimal information about the intended aircraft and its subsystems. To allow moving through wide parameter spectrums, computational effort is kept low.

doi:10.25967/490207

Appropriate methods are comprehensible and trustworthy, however naturally compromise the fidelity level of the tool. As the methods, the overall tool arrangement is intentionally designed easy to keep induction effort for new users low. MATLAB as a widespread programming language among engineers is used.

2.2. Implemented Aircraft Configurations

Four fixed-wing VTOL aircraft configurations are currently implemented in the design tool.

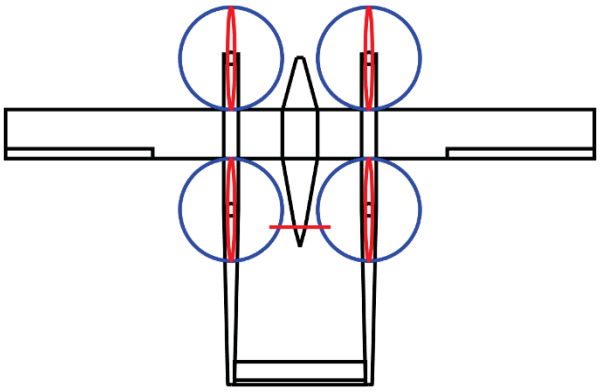

FIG 2. Top View of 'quadXcruise' Configuration

The ‘quadXcruise’ configuration (see FIG 2) represents the most popular fixed-wing VTOL configuration. It uses a conventional twin-boom pusher aircraft and adds a quadrocopter in ‘cross’ (X) orientation to the wings of the aircraft. Hover and cruise powertrains are used in their dedicated flight phases exclusively.

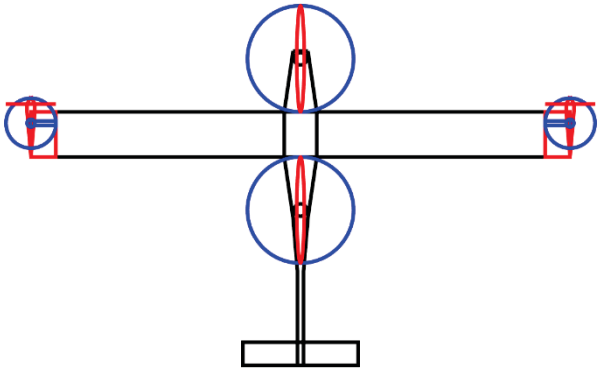

FIG 3. Top View of 'quadPtilt' Configuration

The ‘quadPtilt’ configuration (see FIG 3) was developed at the Institute of Aircraft Design/TU Munich. It is based on a conventional wing-tail configuration. Two hover-only powertrains are attached on top of the fuselage before and aft of the wing. Powertrains are mounted to each of the 120° tiltable wingtip segments. The powertrain arrangement forms a partly tiltable quadcopter in ‘plus’ (P) configuration. The wingtip powertrains are vertical in hover flight to support lift and slightly tilt for yaw control. In wing-borne flight, the fuselage powertrains are inactive and the wingtip powertrains point forward for thrust and yaw control. Roll control is achieved by the antisymmetric deflection of the wingtip segments.

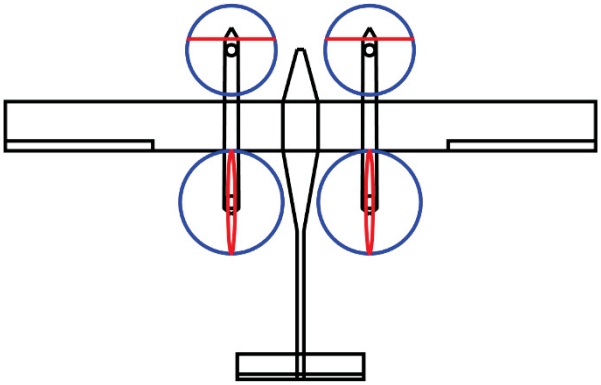

FIG 4. Top View of 'quadXtilt' Configuration

The ‘quadXtilt’ configuration (see FIG 4) has two tiltable powertrains on nacelles before the wing that are used in both hover and cruise. The powertrains behind the wing are solely used for hover and are stopped during cruise flight. Aircraft control in cruise uses conventional control surfaces. In hover, the conventional quadcopter control principle is supported by the tilt capability.

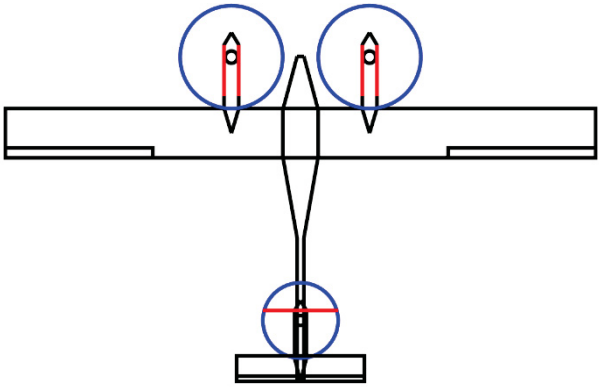

FIG 5. Top View of 'triVtilt' Configuration

The ‘triVtilt’ configuration (see FIG 5) uses two tiltable powertrains in front of the wing and one tiltable powertrain mounted on top and in front of the vertical tailplane. The front powertrains are only used in hover and transition. Their tilting is essential for yaw control in hover. In cruise, the motor axes are tilted horizontal to fold and attach the rotors to the nacelle for drag reduction. Cruise thrust is generated by the rear powertrain. Conventional control surfaces are used.

2.3. Program Structure

Maximizing endurance or range for a given take-off mass is a typical setup for the aircraft design task in the present class and size of aircraft. This enables the program sequence as shown in FIG 6 without relevant time-intense iterations, though increased filter effort to sort out invalid configurations. The principal idea is to subtract all component masses from the target mass until only the battery mass remains. From this energy equivalent, all energy shares of prescribed mission segments e.g. hover

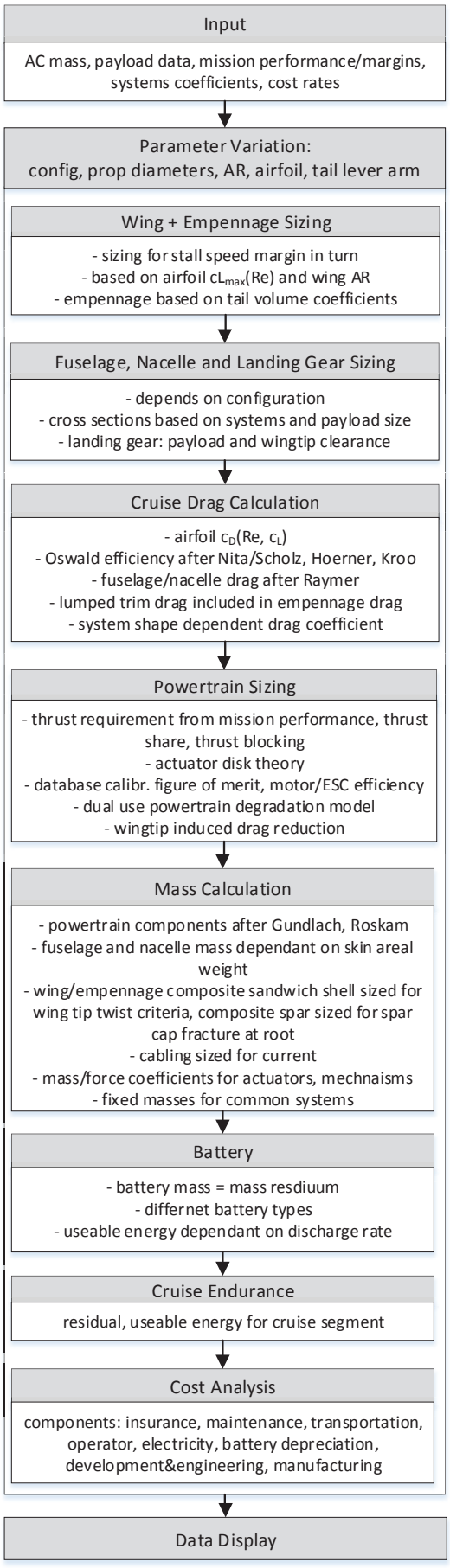

FIG 6. Program Sequence

climb to transition or wing-borne climb is subtracted. The remaining energy is spent on the wing-borne cruise segment from which the endurance or range can be calculated. The component masses derive from structural components or systems that are sized to meet the prescribed mission requirements (e.g. stall speeds, climb rates, transition/cruise altitude). Aircraft are characterized by a few basic parameters like configuration type, aspect ratio, airfoil, etc. Different strategies (e.g. design of experiments, optimization algorithms) can be used to generate the parameter combinations to find a 'best' aircraft. The tool allows to define target functions for this search containing performance as well as cost properties. An exemplary execution time for the program sequence with 22000 aircraft/parameter combinations is 4 min on a single core of a typical desktop computer. All data is stored in intuitive structs that mimic structural and system aircraft layout.

2.4. Mission Segments

The mission consists of the phases 'hover', 'hover climb', 'cruise climb', 'cruise', 'cruise descent' and 'hover descent'. While all hover phases relate to rotor/propeller generated lift with no or low airspeed, all cruise phases relate to wing generated lift with high cruise airspeed. Forward and backward transition from powered to wing lift happens before cruise climb respectively after cruise descent. Transitions are not modelled. For all mission segments except cruise, the duration is either directly defined or by segment altitudes and climb/sink rate. The cruise segment duration is a calculation result. The cruise flight state can contain a prescribed portion of turns or loiter.

2.5. Wing and Empennage Sizing

The wing area is sized to meet a prescribed stall speed at prescribed bank angle. The maximum lift coefficient c_l of the selected airfoil at present Reynolds number is extracted from the inputted airfoil polar data table and transferred to a maximum wing lift coefficient c_L using the lift curve slope formulation in (1).

$$c_L = c_l \frac{AR}{2 + \sqrt{AR^2 + 4}} \quad (1)$$

This requires a short iteration as lift coefficient is depend on wing area via Reynolds number. The applied procedure can only handle a wing without twist, negligible sweep, no/low taper and with constant airfoil along the span. Its validity was checked on exemplary wings whose spanwise lift coefficient distribution was calculated by a lifting line method. Stall was defined as the point when the maximum in local lift coefficient distribution (typically in the wing center/inboard wing section) reached the value of the 2D/airfoil maximum lift coefficient by XFOIL. The maximum wing lift coefficient as calculated in the tool was always near below the

value coming from the validation approach. This leads to a conservatively oversized wing area.

The required polar data tables are generated before executing the tool with XFOIL for the range of lift coefficients and Reynolds numbers. While maximum lift coefficient prediction is taken from XFOIL calculation without change, drag coefficients receive a margin of +15% on top of the XFOIL prediction. This is to account for too optimistic XFOIL results, production inaccuracies and pollution.

Vertical and horizontal tail are sized by prescribed tail volume coefficients and aspect ratios. Hence, tail areas are calculated using the tail lever arm as variation parameter.

For both wing and tailplanes a rectangular planform is used. This simplifying approach is conservative in forecasting structural mass and induced drag. It well approximates UAV wings with high outboard chord lengths due to Reynolds number criticality.

2.6. Fuselage, Nacelle and Landing Gear Sizing

Fuselage and nacelle/motor arm geometry mainly depend on the selected configuration. The bodies are modelled by multiple strung trapezoid or cone segments. Their quadratic or circular cross sections derive from the surrounded components e.g. payload cross section or engine diameter including a spacing margin. Engine diameter is related to the rotor/propeller diameter it is connected to by a database fitted function. Fuselage segment length derive from rotor diameters, wing chord, maximum taper angles and empennage lever arm. The detailed design of predecessor aircraft shows that this procedure mostly ensures sufficient space to store all other components in the correct location and therefore is a reasonable approach for preliminary design. As the battery volume is just calculated at the end, a fit check would imply an iteration or an additional parameter for space reservation and a check at the end. For later use, the area portion of the rotors' downwash cylinder is calculated which is blocked by nacelles or fuselages. The landing gear width is coupled to wingspan while for the height two criteria apply: vertical clearance of the payload bottom to the ground to protect sensible optics and a minimal roll angle defined by the landing gear and the lowest wingtip point to allow for roll angle tolerances during VTOL.

2.7. Cruise Drag Calculation

Aerodynamic drag is only evaluated for the two predominant flight conditions level flight and turn flight. Variations in lift coefficients in the climb/descent segments are neglected due to rather small altitude differences (typ. < 500m) for this type of UAV and the short segment time share. The parasitic drag coefficient c_{D0} is summed up by the aircraft components' contribution and their surface weighting.

$$c_{D0} = \sum_i c_{D0,i} \frac{S_i}{S_{ref}} \quad (2)$$

Assuming that fuselages, nacelles, landing gear, antennas, external payloads, etc. are mounted to experience the angle of attack of minimum drag in the cruise flight condition, their drag can be estimated with only a c_L-independent, zero-lift drag coefficient $c_{D,0}$ term. Accepting some error, this assumption is also used in turn flight despite higher angle of attack.

Fuselage and nacelle drag are calculated with a method presented in [1] that takes into account laminar and turbulent friction coefficients, Reynolds numbers, transition location, body slenderness and interference factors. Landing gear, antenna and payload drag is based on typical drag coefficients of their cross section shape. This is also done for hover powertrains that stand still during cruise flight. [2] provides wind tunnel measurements and validated models to predict drag of rotors resting perpendicular to the airflow, airflow aligned rotors and even retracted rotors. The vertical tail uses the drag coefficient of an exemplary symmetrical airfoil at present Reynolds number. The horizontal tailplane uses a conservative fixed drag coefficient that also covers trim drag. A trim of the pitch moment household is not performed. The drag error caused by inadequate tailplane or trim drag assumptions is typically below the fidelity of the overall tool. Leakage and protuberance drag is considered by a constant factor on the sum of zero lift drag.

The drag estimation of the wing splits up in 2D airfoil drag and 3D drag effects. The wing lift coefficient derives from the cruise flight state and is transformed to an average local airfoil lift coefficient using the inverse form of (1). Together with the Reynolds number in cruise condition, the airfoil drag coefficient is interpolated from the c_l/c_d polar data table. As fuselage-wing or nacelle-wing intersections and propeller outflow trigger turbulent flow, a fixed airfoil drag increase is added in those areas. The overall wing drag coefficient represents zero lift and lift induced drag components on a wing with infinite aspect ratio. An induced drag coefficient $c_{D,ind}$ that represents inviscid, 3D flow effects is added.

$$c_{D,ind} = \frac{{c_L}^2}{\pi\, AR\, e} \quad (3)$$

To cover the different sources of wing induced drag, Oswald efficiency e is calculated in (4) using methods presented in [3], [4], [5] that account for the influences of taper ratio, fuselages/nacelles, dihedral

$$e = e_{taper}\, e_{fusel,nac}\, e_{dihed} \quad (4)$$

[5] provides a function for the Oswald efficiency of unswept, trapezoidal wings with taper ratio λ that can be approximated by a polynomial as in [3]. This formulation hence is not limited to the rectangular wing (λ=1) which is otherwise used in the tool. The degradation of the Oswald efficiency by a fuselage or

nacelle follow an approach after [4] that penalizes the ratio between fuselage width and span. It as well provides a method for the dihedral influence.

The procedure for wing drag calculation uses airfoil polar data that already contains viscid parts of the induced drag. This approach can be considered as more precise than simple formulations that lump various sources of viscid induced drag with a factor K on zero lift drag (e.g. (5)).

$$c_{D,ind} = \frac{c_L^2}{\pi\, AR\, e} + K\, c_{D0}\, c_L^2 \quad (5)$$

Despite not calculating circulation distributions on the wing, the inviscid induced drag component is well describable with a simple formulation of (3) and (4).

2.8. Powertrain Sizing

One powertrain branch consists of the propeller (horizontal thrust) respectively rotor (vertical thrust), the electric motor, the electronic speed controller (ESC) and the connecting cables (see FIG 7). Multiple of those powertrain branches are installed in a fixed-wing VTOL aircraft. The battery is treated separately from the powertrain.

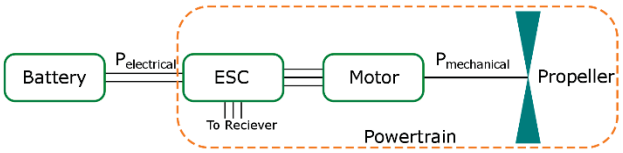

FIG 7. Schematic of an Electric Powertrain [14]

Powertrain sizing starts at the thrust requirements for the individual motor/rotor units i and mission segments j. The total thrust requirement in hover (6) derives an equilibrium of gravity force G and aerodynamic drag in vertical motion $D(\dot{h})$. A thrust share factor $f_{Tshare,i}$ sets the share of total thrust which the dual-use powertrains contribute. A control factor $f_{ctrl,i}$ (e.g. 1.2) adds thrust overhead for vehicle control. This net thrust requirement is corrected for the blocking effects that come from the fuselage or nacelles located in the flow field of the rotor. The blocking factor uses a method described in [6] (see FIG 8) and takes into account the blocked area of the rotor disk $S_{blocked}/A_{disk}$ and the distance of the rotor to the blocking object d/R_{rotor}.

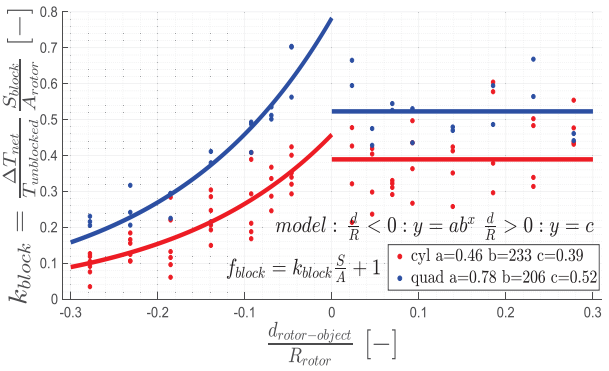

FIG 8. Thrust Blocking Model

$$T_{gross,\,ij} = \frac{(G + D_j(\dot{h}))\, f_{Tshare,i}\, f_{ctrl,i}\, f_{block,i}}{n_{pwtr,i}} \quad (6)$$

Actuator disk theory is used to calculate the required ideal rotor input power. A rotor figure of merit FM = 0.71 and typical operational efficiency of a motor/ESC combination $\eta_{mot,ESC} = 0.8$ were derived from manufacturer data (see FIG 9 as an example).

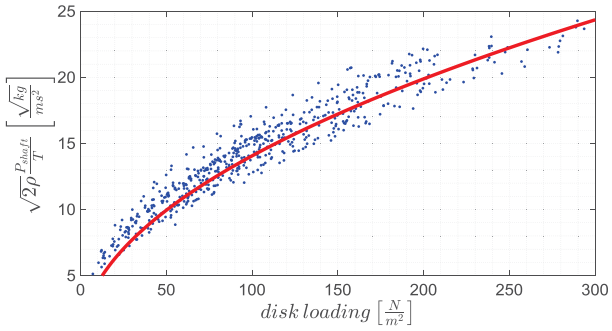

FIG 9. Calibration of Figure of Merit from Measurement Data

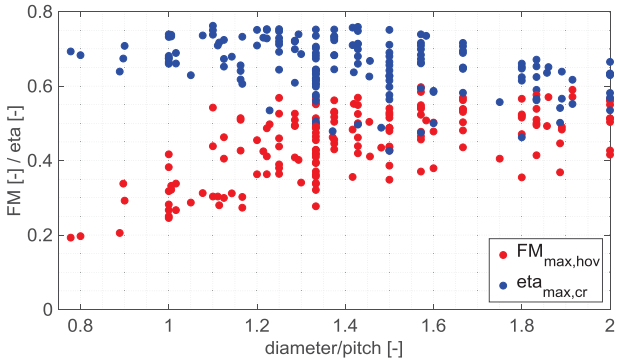

FIG 10. Degradation of Dual-Use Propellers

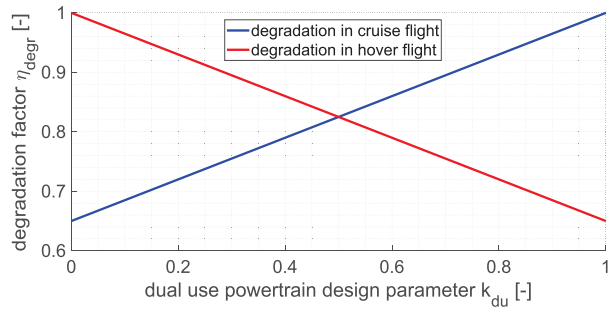

FIG 11. Model to Degrade Dual-Use Powertrains in Off-Design Operation

Powertrains used in both hover and cruise flight show reduced efficiency compared to powertrains being designed and operated in only one of both flight phases. FIG 10 illustrates the encountered efficiency losses for a propeller designed for cruise (diameter/pitch = 1 - 2). Such propeller's figure of merit are as low as 0.4 in hover meaning only 60% of the efficiency of a hover-only rotor. On top of that multiplies the degradation of the motor/ESC due to off design operation. An overall degradation factor of 0.5 to 0.75 seems well possible dependent on the actual operating conditions and powertrain design. To cover this phenomenon, a parameter k_{du} is introduced that describes if the powertrain is designed for hover

($k_{du} = 0$) or cruise flight ($k_{du} = 1$) or somewhere between. Dependent on this parameter, the degradation factor η_{degr} is chosen (see FIG 11).

A further term η_{climb} is used to account for the efficiency degradation during elevated power/off design operation like hover climb. These efficiency figures lead to the electrical power drained from the battery by each powertrain in each mission segment (see (7)).

$$P_{el,ij} = \frac{P_{ideal,ij}}{FM_i \ \eta_{mot,ESC} \ \eta_{degr,i} \ \eta_{climb,j}} \tag{7}$$

For the wing-borne flight phases, the gross thrust requirement is derived from the force equilibrium along the direction of forward motion and, as in the case of hover, shared among powertrains by a factor. Blocking or control overhead is not considered here as it is typically negligible in forward flight. Basic actuator disk theory is modified to cover the worsening of propeller efficiency for very low disk loading DL or high dynamic pressure q by an additional term (see (8) and FIG 12). This expression is calibrated to the 'APC electric' propeller series in the UIUC propeller database [7].

$$\eta_{prop} = \frac{2 \cdot 0.85}{1 + \left(\frac{DL}{q} + 1\right)^{0.65}} \frac{\frac{DL}{q}}{0.036 + \frac{DL}{q}} \tag{8}$$

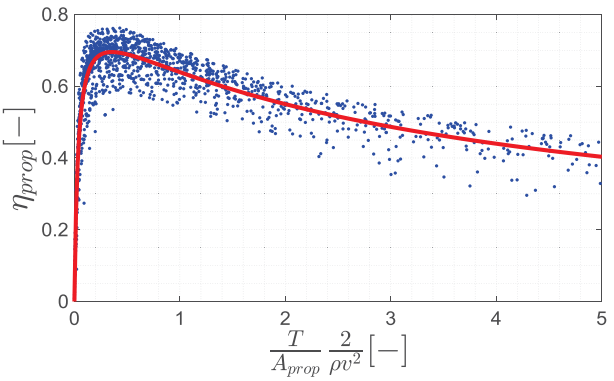

FIG 12. Calibration of Modified Actuator Disk Theory Propeller Efficiency to UIUC database

Fixed values for motor, ESC and miscellaneous powertrain efficiencies are used. The efficiency η_{cfg} allows to degrade propulsive efficiency due to the adverse configuration influence e.g. aft fuselage pusher propulsion. Propulsive efficiency is degraded for elevated power climb segment by η_{climb}. Power drain from the battery in cruise finally is

$$P_{el,ij} = \frac{\left(D + m\,g\,\frac{\dot{h}_j}{v}\right) f_{Tshare,i} \ v}{\eta_{pwtr,i} \ \eta_{prop,ij} \ \eta_{mot} \ \eta_{ESC} \ \eta_{misc} \ \eta_{cfg} \ \eta_{degr,j} \ \eta_{climb,j}} \tag{9}$$

Powertrains mounted at the wingtip and spinning against the wingtip vortex can reduce the wing's induced drag (see [8], [9]). To model this beneficial effect for configurations with the respective powertrain positioning ('quadPtilt'), it is assumed in (10) and (11) that parts of the propellers' swirl power (=lost propeller power) reduce the vorticity that causes parts of the wing's induced drag power $P_{D,ind}$.

$$P'_{D,ind} = P_{D,ind} - f_{tipprop} \, P_{swirl} \tag{10}$$

$$P_{swirl} = \left(1 - \eta_{prop}\right) P_{shaft} = \left(1 - \eta_{prop}\right) \frac{D \, v}{\eta_{prop}} \tag{11}$$

Eliminating airspeed v, dynamic pressure q and wing reference area S_{ref} and rearranging yields the following new, reduced induced drag coefficient $c_{D,ind}'$ in (12).

$$\frac{c_{D,ind}'}{c_{D,ind}} = 1 - f_{tipprop} \frac{\left(1 - \eta_{prop}\right)}{\eta_{prop}} \frac{c_D}{c_{D,ind}} \tag{12}$$

An alternative approach can be found in [10]. $f_{tipprop}$ has to be calibrated to model the efficiency of vorticity reduction by the counter rotating propeller swirl. A value of $f_{tipprop} = 0.085$ is used based on only few inflight measurements made in [6]. It must be pointed out that, in the context of (12), $c_{D,ind}$ only refers to inviscid, 3D flow effects on the wing. In a strict procedure, the new induced drag coefficient $c_{D,ind}'$ would have to be iterated until convergence. For simplicity only one calculation step is made. Overall drag is updated with the new induced drag coefficient $c_{D,ind}'$ and is further used for cruise endurance calculations.

2.9. Mass Calculation

Powertrain components follow established methods after [11] (for electric outrunner motors and ESC) and [12] (for rotors/propellers). To size the cables, the maximum conducted current for each powertrain branch is determined from the individual maximum power and the discharge cut off voltage. A lookup table from [13] provides the mass per length of the cable gauge which is at least required to take the current (in average 1.45 g/m/A per cable string). The cable length can be derived from the aircraft geometry. Overhead is added for non-straight routing, excess length, fixation and electrical connections.

Payload, flight control computer and periphery, actuators, communication systems, etc. are assigned with fixed masses. Cabling of the latter systems is as well considered by constant mass-per-length and the aircraft geometry dependent routing. Tilt mechanisms are modeled as a seesaw based on its geometry. Its mass mainly scales with the square of the motor diameter.

Structural mass of nacelles and fuselages scale with surface area by a factor of 1.05 kg/m². This is well validated for UAV with MTOW around 5 kg with monolithic composite fuselage shell and as well covers internal structure.

Lifting surfaces are designed in composite sandwich shell design and composite I-beam spar construction. For easy analytical sizing, the main load types are

assigned to the following structural components and sizing criteria:

- Wing lift and wing bending is taken by the wing spar. All lift force is introduced at quarter span from the wing root where all aircraft mass is concentrated. Both is a conservative assumption that neglects bending moment reduction by wing mass or wing mounted systems. Lift force is either calculated based on a load factor requirement (wing) or a maximum lift coefficient and airspeed (tailplane). The spar caps are sized for a maximum root bending moment on fiber compression fracture. The shear web of the spar at the wing root is sized for maximum lift force on fiber shear fracture. Hereby, wing stiffness e.g. maximum tip deflection or first bending eigenfrequency is not monitored. Spar caps and shear web linearly taper to one third of their root widths at the wingtip.
- Wing torsion coming from airfoil pitch moments is taken by the wing shell. The layup is sized for a maximum elastic twist at the wingtip of 1° at maximum airspeed. The required layup is symmetrically divided into the face layers of a sandwich to avoid buckling. The layup is the same for the whole wing. Minimum layer thickness is defined by fabrics currently available on the market.

Typical carbon fiber material properties are used. Additionally, bonding masses, additional control surface shear webs and paint are considered in mass.

The applied method can be considered as a simplified version of [14], [15], [16].

2.10. Battery Modelling

A single battery supplies all powertrains as well as the systems and payload in all flight phases. In high power flight phases like hover climb, it needs to provide almost one magnitude more power than is required for wing-borne cruise flight. Here however, it shall provide maximum energy for its mass. This is a challenging trade-off for a battery (as FIG 13 shows) with significant impact on electric VTOL performance.

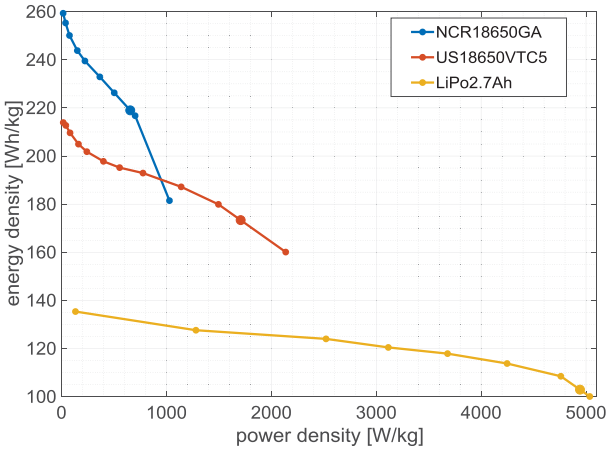

FIG 13. Batteries' Trade of Energy Density vs. Power Density

The three curves show the trade between energy density and power density per cell design/chemistry and applied discharge rate. Each small point represents the averaged power respectively cumulated energy over a complete constant current discharge to cutoff voltage. A high energy Panasonic NCR18650GA lithium ion battery (blue) provides significantly more energy for the same mass than a typical RC hobby lithium polymer battery (yellow), but at the cost of significantly reduced maximum power capability. The manufacturer rating for maximum sustained power capability at cutoff voltage is marked by the big dots. Within one curve, it can be seen that the useable energy degrades with increased power drain. The upper two batteries (lithium ion cells) show a higher sensitivity towards this effect loosing up to 20% of their useable energy at maximum discharge rate.

To model this essential effect in a convenient way, a battery efficiency η_{bat} is introduced.

$$\eta_{bat} = \frac{E_{bat}(P)}{E_{bat}(P \rightarrow 0)} \tag{13}$$

It relates the reduced useable energy battery due to a high power drain with the useable battery energy for the hypothetical ‘zero power’ drain case. In that way, each mission segment (which is assumed to have constant power drain) gets assigned its battery efficiency η_{bat} . Battery energy shares are consequently expressed as “internal” battery energy, as if discharge rate approaching zero were used. Battery data containing the battery efficiencies are inputted as lookup tables.

The applied model uses power drain instead of the usual current drain as the source of useable battery energy degradation. Dependent on the state of charge voltage, the same power can be provided at different currents and affect energy degradation differently. What argues against this inaccuracy is the averaging character of the used data for battery efficiency determination throughout a discharge cycle.

Due to the high capacity of lithium ion cells in relation to the total battery pack capacity of small aircraft, a battery pack only consists of few parallel cell strings. Consequently, the energy steps in which battery packs can be manufactured are significant. E.g. going from a 6s4p to the next bigger 6s5p cell connection means +25% in energy and mass. Therefore, batteries are discretely sized respecting possible cell interconnections.

To consider additional mass for battery cell assembly, protection case, battery management system and power connectors, a mass factor f_{pack} of 1.1 is used. For battery life extension, only $f_{lifeext}$= 80% of the total battery capacity is used for a mission.

2.11. Cruise Endurance Calculation

After all systems and structural masses are subtracted from the required take-off mass, the mass of the battery remains. The energy that is left after subtraction of the time-fixed mission segment energies is available for cruise propulsion and system supply. With the knowledge of this overall power P_c, the cruise endurance t_c is calculated.

(14) $$m_{bat} = m_{total} - \sum m_{sys} - \sum m_{struct}$$

(15) $$E_{c,int} = \frac{f_{lifeext}}{f_{pack}} m_{bat} \left.\frac{E}{m}\right|_{cell} - \sum_{msn\ seg} \frac{E}{\eta_{bat}}$$

(16) $$t_c = \frac{E_{c,int}\ \eta_{bat,c}}{P_c}$$

2.12. Cost Analysis

To establish a simple, though meaningful cost analysis for the beforehand designed fixed-wing VTOL aircraft, cost components of development, manufacturing, operation and maintenance are considered. The underlying business chain is depicted in FIG 14. The 'UAV Company' develops the aircraft and sells it to a 'UAV Service Provider' that conducts flight missions to gather e.g. imagery data or transport a good in the name of the 'Customer'.

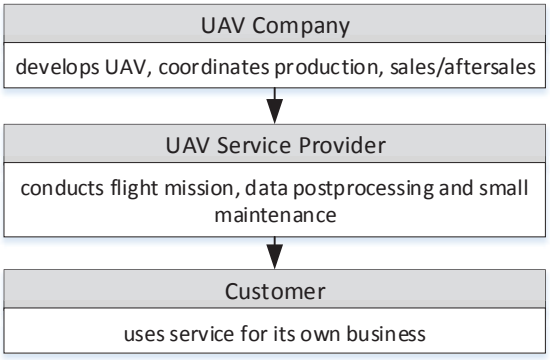

FIG 14. Business Chain

As the aircraft design itself, the cost analysis requires a number of input to properly represent the production and operation circumstances. Perhaps more than with the aircraft design, the input numbers may only be valid for a very narrow range of aircraft size.

2.12.1. Production

Production cost of an aircraft sum up from tooling, component and raw material cost, and labor cost for production, integration, setup, checks and flight test.

Wherever possible the raw material or component cost relate to number of components and their properties like dimensions or power capability. Based on that, per unit or per property prices (e.g. 0.35 €/W for powertrains including propeller, motor, and ESC for 5 kg aircraft) are multiplied. To estimate labor cost, duration of production steps are defined and scale with the number of step repetitions (e.g. powertrain integration) or size of parts (e.g. composite layup). Manufacturing labor rate includes workshop environment and overhead cost, and range from <5 €/h (China) to 55 €/h (Western Europe).

2.12.2. Development and Engineering

Development and engineering cost is made up based on the time to develop system units (e.g. 3 man months for a powertrain, 3 man months for a tilt mechanism, 1.5 man months for a control surface), their frequency and the labor rate. A component of general development effort scales with the aircraft mass without payload and a rate of 6 man months per kg. The applied labor rate is 12000 €/man month. Cost for several prototypes (derived from aircraft production cost) add on top of the labor cost. This total cost is shared by the estimated number of produced aircraft (500). Development and engineering cost is likely the most vague and least predictable cost component of the ones presented here. Company data on development program cost is hardly accessible and poorly traced.

2.12.3. Acquisition and Depreciation

Cost for the complete aircraft system purchase add up from development, production, ground control station, payload and transportation/turn around equipment. Overhead factors for administration and sales departments of the development and production company multiply on top as well as potential interest cost and profit margins. A simple linear depreciation model divides the above cost of system components by the applicable operation hours or number of missions until end of life.

The purchase and disposal cost of the battery are linked to its energy content (0.833 €/Wh). It depreciates linearly with the number of charge-discharge cycles until it has to be renewed (300). One cycle per mission flown is assumed.

2.12.4. Maintenance

An exemplary maintenance program is set up consisting of types of checks with different time effort, replacement cost and intervals. While the 'small' check is limited to thorough visual checks, cleaning and relubrication, the 'big' check involves exchange of wear prone components like actuator gears or engine bearings. Cost is again made up from time for work step, repetition of work steps and labor rate plus replacements part cost.

2.12.5. Electricity

Electricity to recharge the battery depends on the energy used within a flight mission. An electricity price of 0.2916 €/kWh and a charging efficiency of 0.95 is assumed.

2.12.6. Operating Personnel

Cost for personnel to conduct the actual flight mission builds up from number of personnel for a subtask,

time for conduct a subtask and the personnel's labor rate (60 €/h). Subtasks involve installation of the payload (2 min), transportation to/from take-off site (one way 25 km, 0.15 €/km, 80 km/h), rigging/unrigging of aircraft (10 min), exchange of battery (4 min), flight trajectory definition (10 min), preflight checks (20 s), monitoring the actual flight, data post processing (1 h) to make it useable for the customer.

2.12.7. Insurance and Permissions

Insurance for the aircraft itself and the payload make up with 0.025% of aircraft and payload cost per year. Insurance against damage to third parties and flight permissions calculate with a fixed rate of 150 €/year. Yearly costs are allocated by an assumption of 150 missions per year.

2.12.8. Cost for Customer

The cost for a land survey or transport mission is given in €/ha or €/kg/km. On top of the internal costs for the service provider company add overheads for administration, sales (together +35%) and profit (+50%).

3. EXEMPLARY TOOL RESULTS

In the following exemplary tool results are presented to give insights in the aircraft configurations and their performance. Within reasonable ranges, discrete values of the parameters

- rotor/propeller diameters
- wing aspect ratio
- tailplane lever arm
- dual-use powertrain design parameter k_{du}
- thrust share of dual-use powertrains of total hover thrust $f_{Tshare,hov}$

are combined and inputted into the tool. The presented aircraft achieve the best endurance among their configuration. TAB 1 provides an overview of the most relevant input and output parameters.

Input

aircraft [mass kg]	5
payload mass [kg]	0.8
cruise airspeed [m/s]	20
stall airspeed at 45° bank [m/s]	17
time in hover/hover climb/cruise climb [s]	20/17/67
battery serial connection	6s
area of survey [ha]	200
swath width [m]	100

Results

	quadPtilt	quadXcruise	quadXtilt	triVtilt
span [m]	2.34			
aspect ratio [-]	14			
airfoil	SD7037			
prop diameter hover/cruise [in]	26/8	18/9	12/8	16/10
battery	6s5p-GA		6s5p-VTC5	
cruise glide ratio [-]	15.5	14.9	16.1	17.7
max cruise endurance [min]	95	94	71	79
powertrain efficiency cruise [-]	0.484	0.477	0.481	0.487
k_{du} [-]	1	-	1	1
$f_{Tshare,hov}$ [-]	0.1	-	0.3	0.3
cost manufact/delevop, no company overheads [€/AC]	4480/ 1336	4508/ 1339	4848/ 1431	4719/ 1423

TAB 1. Tool In- and Outputs

All aircraft use the same aspect ratio of 14 (note: stepwidth of 2) which is within a typical range for RC motor gliders of that size. The battery cells are connected 6s5p with every aircraft. The battery cell type however differs. The maximum power requirement (see FIG 15 'totalmax/req bat') decides which battery type is useable. Only for 'quadPtilt' and 'quadXcruise', the power requirement can be designed just low enough to use the most energy-dense GA battery type (see also FIG 16, GA = 1). The maximum power requirement is set by the power requirement in hover climb ('pwtr hc') plus a minor system/payload power. The power requirement at the beginning of transition (hover + forward acceleration) may be higher than in hover climb. It is however only present very shortly, so that it is considered to be taken by the short-term overpower capability of the battery. The 'quadXcruise' configuration with its four large, hover optimized rotors undercuts the power limit with reasonable rotor size while 'quadPtilt' is driven to unusual large rotor for its weight category. The power penality of the fully cruise optimized dual-use powertrains (k_{du} = 1) is low due to its low thrust loading ($f_{Tshare,hov}$ = 0.1 , also represents limit for

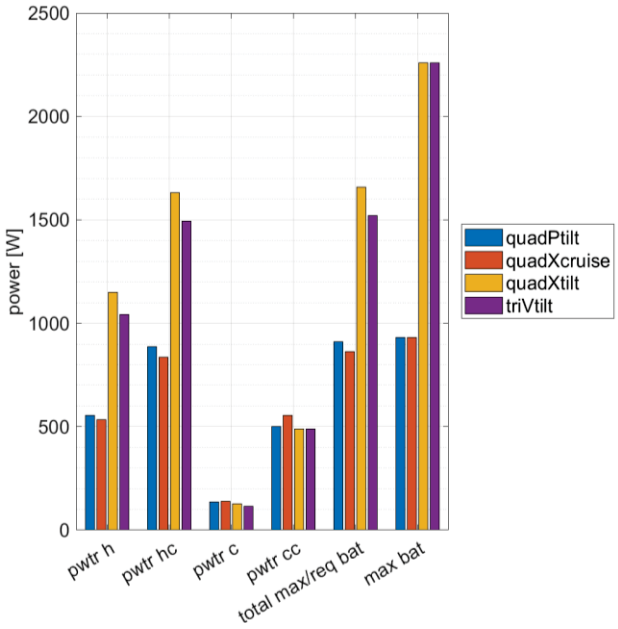

FIG 15. Power Breakdown

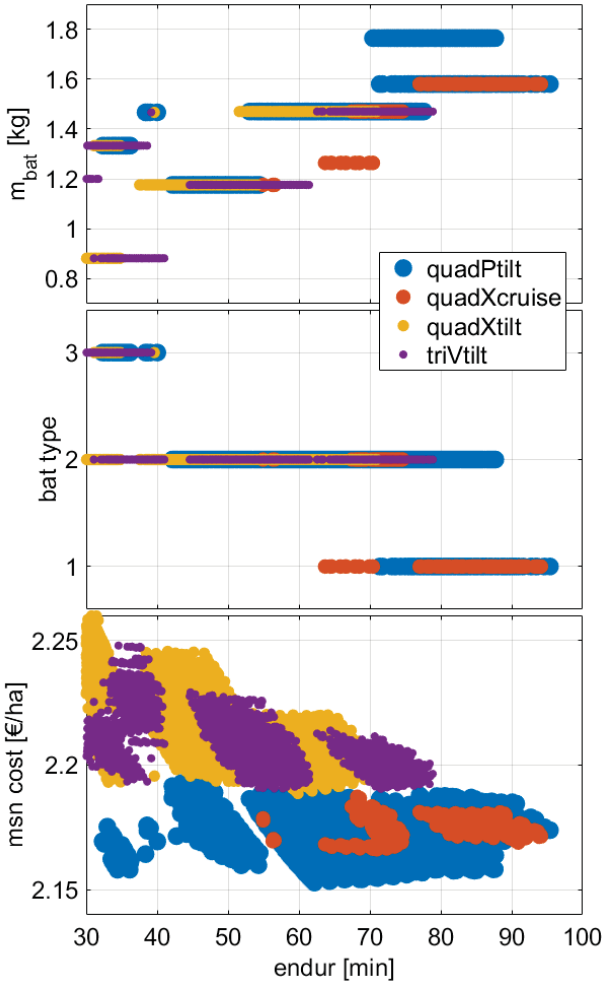

FIG 16. Total Population/Sensitivity Plots

sufficient controllability). For ‘quadXtilt’ and ‘triVtilt’, all possible powertrain designs exceed the power capability of the highest energy-density battery type. The use of highly loaded, inefficient dual-use

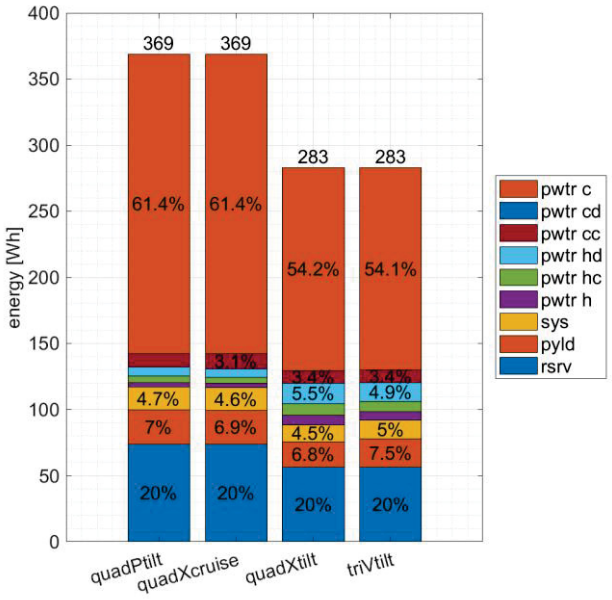

FIG 17. Energy Breakdown

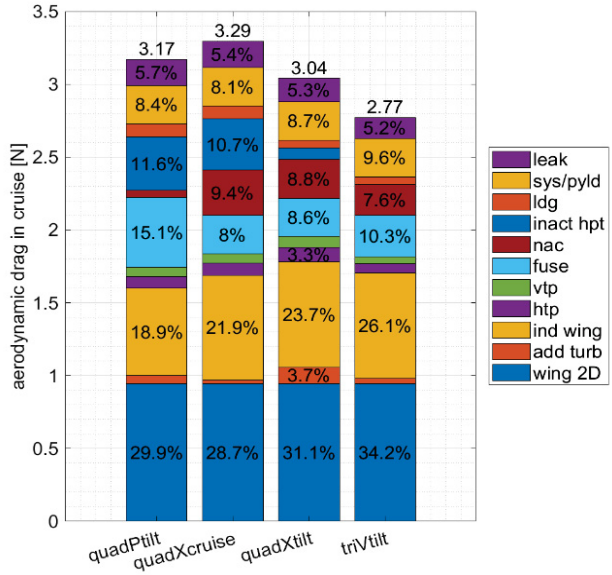

FIG 18. Drag Breakdown

powertrains and low number of rotors, respectively, are the cause. In return, the higher power capability of their batteries give design freedom towards enhanced the cruise performance. The increase in onboard energy when using the more energy-dense battery type at the same battery interconnection is enormous (see FIG 17). Due to the short durations, the configurations’ differences in hover power consumption do not remarkably affect its share of overall batter energy. After these time-fixed flight phases and the reserve, more than 40% more energy is available for cruise. To efficiently convert this energy into cruise endurance (= optimization target) all cruise powertrains are fully optimized for cruise. This design freedom is present as the powertrains are either only active in cruise (‘quadXcruise’), do not relevantly contribute to hover power (‘quadPtilt’) or hover power is irrelevant as energy-dense batteries

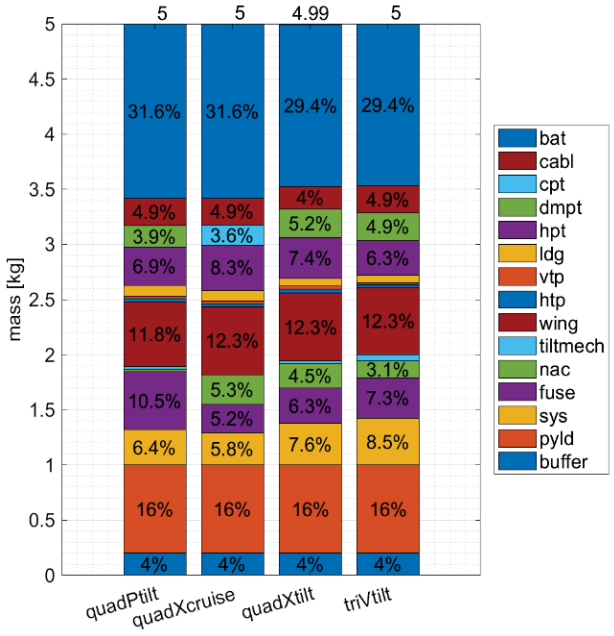

FIG 19. Mass Breakdown

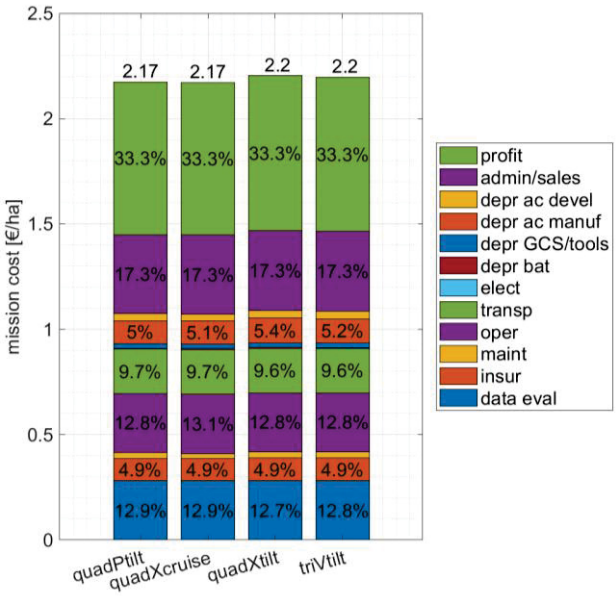

FIG 20. Mission Cost Breakdown

cannot be used anyhow.

The glide ratio and with that, the drag estimation, settles at reasonable values for this size and kind of aircraft. The drag breakdown (see FIG 18) shows that wingtip propulsion saves roughly 17% in induced drag against the other configurations with identical aspect ratio. 'quadXtilt' suffers most from additional turbulent drag triggered by propeller outflow. Fuselage and nacelle drag together are roughly the same for all configurations. The drag of the inactive hover powertrains of the low-hover-power configurations make up remarkable 11% of the total airframes drag. Mainly because this drag item is not present with 'triVtilt' its glide ratio outperforms the rest. Glide ratio or cruise powertrain efficiency however can by far not make up for the lower available energy so that the 'quadPtilt' and 'quadXcruise' achieve 25% more in cruise endurance over 'quadXtilt' and 'triVtilt'. FIG 16 shows that by using battery type 2 /VTC5 still 91% of cruise endurance is achievable for a 'quadPtilt' configuration by managing to increase battery mass. Its parameters are AR= 12, $d_{rot/prop}$ = 16/10, L/D = 17, eta_{cr} = 0.455, k_{du} = 1, $T_{shr,hov}$ = 0.3. All other configurations cannot shift sufficient mass to install a heavier battery. As with the drag, fuselage and nacelles together make up for about the same mass fraction with all configurations (see FIG 19). Additional, heavy tilt actuators drive the systems mass with 'quadXtilt' and 'triVtilt'. No significant mass differences are visible between total powertrain masses of configuration with high and low power consumption in hover. Naturally, the selection for the best aircraft reduces residual mass to a minimum. The resulting overall mass consequently does not differ significantly from the initial mass requirement on which most calculations rely on.

With regard to cost, manufacturing and developing of either aircraft is comparable (see TAB 1). Extended for sales and profit overheads, the costs well agree with typical market prices. The cost breakdowns of the endurance optimized aircraft (see FIG 20) for the roughly 30 min long survey mission show per-area end prices for a customer within a narrow range of 1%. The shares of configuration driven items like energy consumption or maintenance are small. Apart from company and profit overheads, the biggest shares in prime cost like data evaluation, operator cost or transportation (including the driver) are driven by personnel cost. Insurance and depreciation of the aircraft cause 5% shares. From FIG 16 can be seen that cruise endurance optimization and mission cost optimization do not completely go in hand. The lowest cost aircraft is of 'quadPtilt' configuration and does only achieve 62 min of maximum cruise endurance. The reason is e.g. a reduced battery and airframe size. Cost between best endurance and best cost aircraft however barely differ (~1%). All aircraft capable of the 30 min mission range within 5% of per-area cost.

4. CONCLUSION

Several conclusions can be taken out for the make of a VTOL design tool, VTOL aircraft design and business cases involving such aircraft.

Certainly the most sensible parameter for aircraft performance is the battery type. Looking for more battery types with characteristics between the three implemented ones is smoothing the results. However, the contradiction between power capability and energy density is inherent in battery design and is further pronounced for future super high energy density cells. Battery architectures mixing high power and high energy battery cells may appear as a feasible workaround.

For single battery architectures as in this paper, the

modelling of the maximum power consumption is critical. Momentum theory is well calibratable to measurement databases. Fixed motor and ESC efficiencies trust in the powertrain designer to select components that achieve these values for all configurations. A most simple degradation model covers powertrains with multiple, strongly differing operating conditions. Despite its rather pessimistic calibration, the tool selects fully cruise optimized powertrains. This might indicate that a complex multi operation point powertrain detailed design is often not required. A modelling of rotor thrust blocking supports hover power prediction. Its effect is however only becomes important for configurations with small rotor areas or wide nacelle cross sections.

An alternative, however less effective strategy besides using highest energy density cells along with low power hover aircraft is freeing mass for more battery out of the relaxed maximum power requirement. Additional mass can be gained from items that do not directly scale with hover power. Examples are lighter fixed mass items (e.g. fewer actuators by functionality integration) and low structural mass (e.g. no additional nacelles). As well, dual-use powertrains are advantageous over separated hover and cruise configurations in this regard.

For the examined scale of aircraft, the feasible battery interconnections cause significant steps in battery energy. Their discrete modelling is strongly advised. The degradation of useable battery energy with discharge power turns out to be relatively irrelevant for the present study. Time shares of high power flight phases are too short to generate significant energy shares. And discharge rates in cruise are low and within narrow ranges for all the configurations.

Drag prediction fits within historical reference data. The highest share of airfoil drag (30% of total) is appropriately modelled with increased fidelity polar data. The 20% share of induced drag related to inviscid 3D effects may be worth extra computational effort for more precise modelling. Calculating lift distribution would as well improve stall and wing area prediction. A simple model allows to incorporate induced drag saving due to wingtip propulsion. The calculated savings seem to be too optimistic. A proper validation of the model must be performed. The high drag share of inactive hover rotors with the best performing configurations proposes further performance potential when using systems to reduce this drag.

Mass modelling can be considered as sufficiently precise. With respect to a 4% share in total mass, the often neglected modelling of cabling is essential for distributed electric propulsion vehicles.

The generated cost breakdowns give insight in the cost structures. The highest cost shares of company administration/sales overhead and profit have potential for more detailed modelling. They however highly depend on the company structure and philosophy. The impact of aircraft design in terms of general geometry or powertrain design (e.g. fixed rotor vs. tilt rotor) does not significantly affect cost items like maintenance, manufacturing or development cost. Detailed aircraft and toolchain design that influences personnel cost is rather crucial. Examples are designs for quick handling like rigging without tooling, automated trajectory generation or data post processing. The solutions must allow a single operator to perform these tasks. Replacing transportation by flying to the deployment site from a central location would mean a significant cut in cost. Also multiple aircraft could perhaps be monitored by a single operator. Maximum endurance gets relevant when it is required to fully exploit it for a mission. The associated effect of lower energy consumption is irrelevant in the context of low energy cost. The estimate of per-area cost allows to judge on the profitability of business cases UAV survey flights. The investment of roughly 2.2 €/ha must be compensated by e.g. a farmer's saving in fertilizer or increase in crop yield.

5. REFERENCES

[1] D. P. Raymer, Aircraft Design: A Conceptual Approach, Blacksburg/VA: AIAA, 2012.

[2] P. Stahl, C. Roessler and M. Hornung, "Benefit Analysis and System Design Considerations for Drag Reduction of Inactive Hover Rotors on Electric Fixed-Wing VTOL Vehicles," in *AIAA Aviation*, Atlanta/GA, 2018.

[3] M. Nita and D. Scholz, "Estimating the Oswald Factor from Basic Aircraft Geometrical Parameters," in *Deutscher Luft- und Raumfahrtkongress 2012, DocID: 281424*, Berlin, 2012.

[4] I. Kroo, "Drag Due to Lift: Concepts for Prediction and Reduction," *Annual Reviews, Fluid Mechnaics, Vol. 33,* 2001.

[5] S. F. Hoerner, Fluid-Dynamic Drag, Bakersfield, CA: Hoerner Fluid Dynamics, 1965.

[6] P. Stahl, C. Roessler and M. Hornung, "Configuration Redesign and Prototype Flight Testing of an Unmanned Fixed-Wing eVTOL Aircraft with Under-Fuselage Hover Lift and Pusher Wingtip Propulsion System," in *VFS Autonomous VTOL Technical Meeting and Electric VTOL Symposium*, Mesa/AZ, 2019.

[7] J. B. Brandt and M. S. Selig, "Propeller Performance Data at Low Reynolds Numbers," in *AIAA Aerospace Science Meeting*, Orlando/FL, 2011.

[8] M. Dimchev, "Experimental and Numerical Study on Wingtip Mounted Propellers for Low

Aspect Ratio UAV Design," Delft University of Technology, Delft, 2012.

[9] J. C. Patterson and G. R. Bartlett, "Effect of a Wing-Tip Mounted Pusher Turboprop on the Aerodynamic Characteristics of a Semi-Span Wing," in *AIAA/SAE/ASME/ASEE 21st Joint Propulsion Conference*, Monterey/CA, 1985.

[10] A. M. Stoll and G. V. Mikic, "Design Studies of Thin-Haul Commuter Aircraft with Distributed Electric Propulsion," in *16th AIAA Aviation Technology, Integration, and Operations Conference*, Washington, D.C., 2016.

[11] J. Gundlach, Designing Unmanned Aircraft Systems: A Comprehensive Approach, Blacksburg/VA: AIAA, 2012.

[12] J. Roskam, Airplance Design, Part V: Component Weight Estimation, Lawrence/KS: DARcorp., 1989.

[13] S. Oberschwendtner, C. Roessler and M. Hornung, "Multi Objective Optimization of Wiring Harnesses for Overall System Performance of Electric Fixed Wing VTOL UAVs," in *VFS Autonomous VTOL Technical Meeting and Electric VTOL Symposium*, Mesa/AZ, 2019.

[14] C. Rößler, Conceptual Design of Unmanned Aircraft with Fuel Cell Propulsion System, München: Verlag Dr. Hut, 2012.

[15] T. Seren, C. Roessler and M. Hornung, "Comparative eVTOL UAV Design Optimization," in *VFS Autonomous VTOL Technical Meeting and Electric VTOL Symposium*, Mesa/AZ, 2019.

[16] P. Stahl, T. Seren, C. Roessler and M. Hornung, "Development and Performance Comparison of Optimized Electric Fixed-Wing VTOL UAV Configurations," in *ICAS Conference 2018*, Belo Horizonte, Brazil, 2018.

[17] M. Thiele, M. Obster and M. Hornung, "Aerodynamic Modeling of Coaxial Counter-Rotating UAV Propellers," in *8th Biennial Autonomous VTOL Technical Meeting*, Mesa/AZ, 2019.